UC Berkeley
UC Berkeley Previously Published Works

Title
SiX2 (X = S, Se) Single Chains and (Si—Ge)X2 Quaternary Alloys

Permalink
https://escholarship.org/uc/item/8t13b78k

Journal
ACS Nano, 18(27)

ISSN
1936-0851

Authors
Lee, Yangjin
Choi, Young Woo
Li, Linxuan
et al.

Publication Date
2024-07-09

DOI
10.1021/acsnano.4c04184

Peer reviewed

ARTICLE

SiX$_2$ (X = S, Se) Single Chains and (Si−Ge)X$_2$ Quaternary Alloys

Yangjin Lee,*,$^{\nabla}$ Young Woo Choi,$^{\nabla}$ Linxuan Li, Wu Zhou, Marvin L. Cohen, Kwanpyo Kim,* and Alex Zettl*

Cite This: ACS Nano 2024, 18, 17882−17889

Read Online

ACCESS | Metrics & More | Article Recommendations | SI Supporting Information

ABSTRACT: Layered or chain materials have received significant research attention owing to their interesting physical properties, which can dramatically change when the material is thinned from bulk (three-dimensional) to thin two-dimensional sheet or one-dimensional (1D) chain form. Materials with the stoichiometry AX$_2$ with A = Si or Ge and X = S or Se form an especially intriguing semiconducting class. For example, bulk silicon dichalcogenides (SiX$_2$) consist of 1D chains held together by van der Waals forces. Although this structural configuration has the potential to reveal interesting physical phenomena within the 1D limit, obtaining SiX$_2$ single chains has been challenging. We here examine experimentally and theoretically SiX$_2$ materials in the low chain number limit. Carbon nanotubes serve as growth templates and stabilize and protect the structures, and atomic-resolution scanning transmission electron microscopy directly identifies the atomic structure. Two distinct chain structures are observed for SiX$_2$. Si$_x$Ge$_{1−x}$S$_{2(1−y)}$Se$_{2y}$ quaternary alloy chains are also synthesized and characterized, demonstrating tunable semiconducting properties at the atomic-chain level. Density functional theory calculations reveal that the band gap of these alloy chains can be widely tuned through composition engineering. This work offers the possibilities for synthesizing and controlling semiconductor compositions at the single-chain limit to tailor material properties.

KEYWORDS: one-dimensional materials, silicon dichalcogenides, nanotubes, atomic chain, transmission electron microscopy, density functional theory
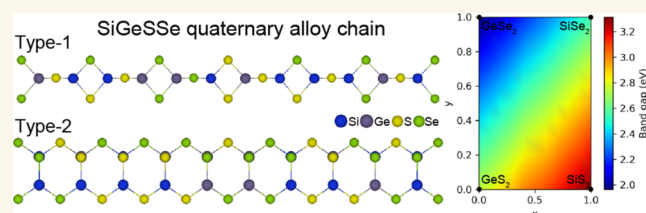
INTRODUCTION

The investigation of reduced dimensionality materials has aroused intensive experimental and theoretical interest owing to their extraordinary physical characteristics, such as optical, electrical, thermal, and magnetic properties, which differ significantly from those of bulk forms.[1−6] In particular, one-dimensional (1D) materials, including nanowires, nanorods, and nanotubes, have garnered considerable attention owing to their potential applications in nanoelectronics, nanodevices, nanocomposite materials, Li-ion batteries, and nanophotonics.[7−11] Recent advances in the study of van der Waals (vdW) two-dimensional (2D) materials have led researchers to investigate the less-explored area of vdW 1D materials.[12−14] vdW 1D materials are composed of molecular/atomic chains with strong intrachain covalent or ionic bonds and relatively weak interchain vdW interactions. This structural configuration, particularly the presence of vdW gaps in 1D materials, offers enhanced flexibility for structural manipulation and modification, and it is completely free from the limitations imposed by the strong covalent bonds in nominally three-dimensional (3D) materials.[12]

Silicon or germanium dichalcogenides (AX$_2$, A = Si or Ge and X = S or Se) are examples of vdW 1D chain structures with semiconducting properties. The bulk crystal structure of SiS$_2$ and SiSe$_2$ consists of edge-shared SiS$_4$ and SiSe$_4$ tetrahedral chains interconnected via vdW forces (Figure 1a).[15−17] This atomic arrangement can lead to interesting physical phenomena as the thickness (number of chains) decreases. However, investigations of these materials at the single-chain level have been limited because of their poor environmental stability. Moreover, the formation of a ternary alloy structure (SiSSe) via the combination of SiS$_2$ and SiSe$_2$ illustrates the possibility of tailoring physical properties such as band gap by adjusting the alloy composition ratio.[18] Although considerable research has focused on manipulating these properties via changes in
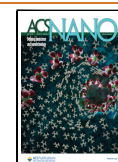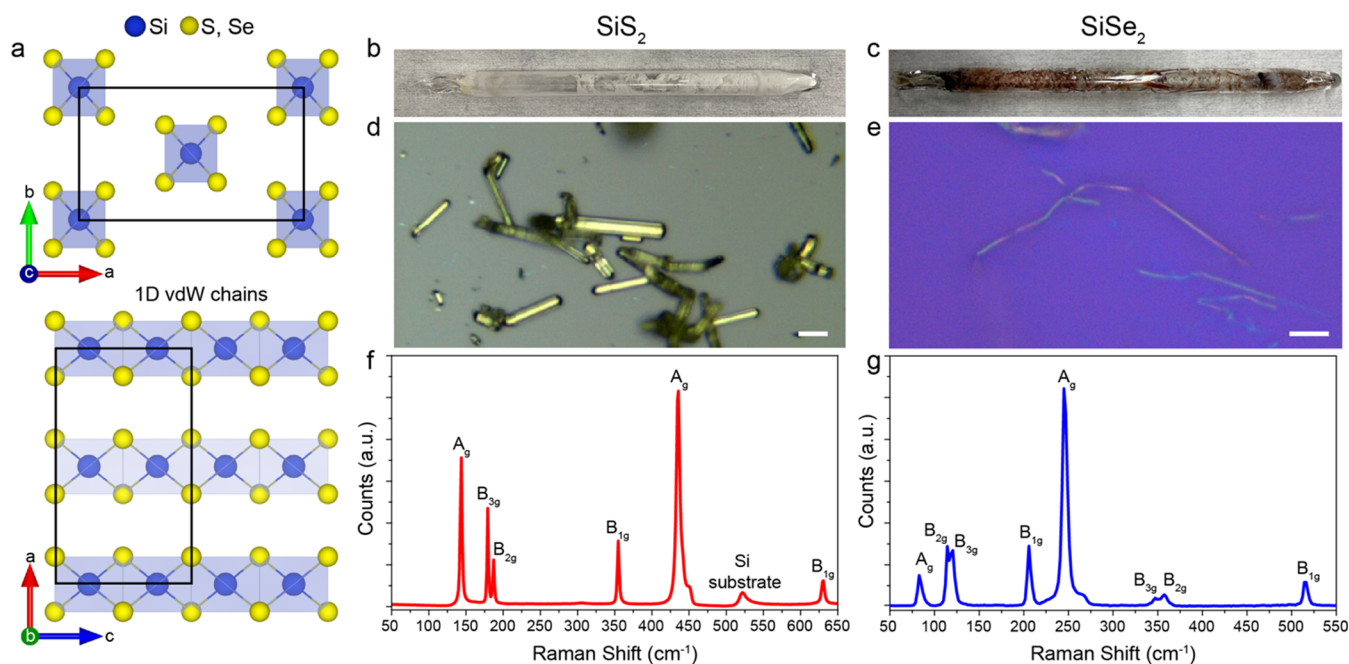
Figure 1. Bulk SiX$_2$ synthesis and characterization. (a) Crystal structure of Bulk SiX$_2$. The single chain consists of the edge-shared SiX$_4$ tetrahedrons (silicon atoms blue, chalcogen atoms yellow). (b, c) Photos of the synthesized (b) SiS$_2$ and (c) SiSe$_2$ inside ampules. (d, e) Optical image of (d) SiS$_2$ and (e) SiSe$_2$ micro wires on SiO$_2$/Si substrate. Scale bar: 20 and 5 μm, respectively. (f, g) Raman spectra of synthesized (f) SiS$_2$ and (g) SiSe$_2$.

the alloy composition, research on the single-chain limit is still lacking. Alloying in the single-chain limit may also be extended by incorporating analogous tetrahedral systems such as germanium chalcogenide tetrahedrons (GeS$_4$ and GeSe$_4$) to create quaternary alloy structures with diverse compositions. The realization and in-depth characterization of these alloy compositions can reveal their interesting material properties and application ranges by broadening the utility spectrum of vdW 1D materials.

The use of carbon nanotubes (CNTs) and boron nitride nanotubes (BNNTs) as reaction templates for encapsulation has proven highly effective for synthesizing various nanostructures.[19−23] This innovative method enables the creation of a diverse array of vdW 1D materials by introducing various substances such as monoelements, perovskites, metal halides, carbides, and chalcogenides into the confined spaces of nanotubes.[24−36] In particular, the small inner diameter of the nanotubes is advantageous for synthesizing 1D chain structures because it limits the radial growth of the encapsulated material. This geometric confinement effect of nanotubes has provided the opportunity for the emergence of crystal structures and properties not found in their bulk form.[37−40] Furthermore, the protective sheaths formed by the nanotubes play a crucial role in shielding the encapsulated materials from degradation, thereby facilitating the investigation of various nanostructures. Consequently, the nanotube encapsulation method serves as a powerful and effective technique for the production of vdW 1D nanostructures and offers the potential for utilizing these materials in various technological areas.

Here, we demonstrate the stabilization of individual SiX$_2$ chains in CNTs, including Ge-containing alloy compositions. Encapsulation in nanotubes significantly enhances the environmental stability of single chains, thereby enabling their comprehensive characterization. Atomic-resolution scanning transmission electron microscopy (STEM) reveals the detailed

atomic structure, and we observe two distinct types of SiX$_2$ chains. Moreover, we synthesize and characterize the Si$_x$Ge$_{1−x}$S$_{2(1−y)}$Se$_{2y}$ quaternary alloy chains, demonstrating their tunable semiconducting properties at the atomic-chain level. Density functional theory (DFT) calculations identify the electronic structures of these alloy chains and reveal their widely tunable electrical properties. This work provides possibilities for synthesizing and controlling the composition at the single-chain limit to tailor material properties.

RESULTS AND DISCUSSION

Bulk SiS$_2$ and SiSe$_2$ are directly synthesized using the melt-growth methods (see Methods section). Figure 1b,c shows the as-synthesized SiS$_2$ and SiSe$_2$ samples inside quartz ampules, respectively. The SiS$_2$ samples exhibit small, thin, white powder-type crystals, whereas SiSe$_2$ samples exhibit red-brown, needle-shaped crystals. The morphologies of the samples are characterized by optical microscopy (Figure 1d,e). SiS$_2$ displays individual wires of a few micrometers, whereas SiSe$_2$ shows a bundle of millimeter-sized crystals. Raman spectroscopy measurement is performed to identify the phase of SiS$_2$ and SiSe$_2$. Figure 1f,g shows the Raman spectra of the crystalline SiS$_2$ and SiSe$_2$, respectively. The Raman peaks (144, 180, 187, 355, 436, and 630 cm^{-1}) from SiS$_2$ and (83, 114, 120, 206, 245, 346, 357, and 515 cm^{-1}) from SiSe$_2$ are obtained. The observed highly intensive and narrow peak at 437.4 cm^{-1} for SiS$_2$ and 244 cm^{-1} for SiSe$_2$ corresponds to the A_g symmetric stretching mode of SiX$_4$, which suggests that the synthesized product is highly crystalline.[16,17] All of the observed Raman peaks of SiS$_2$ and SiSe$_2$ are assigned and matched well with previously reported Raman results.[18]

The SiS$_2$ and SiSe$_2$ samples exhibit high reactivity to ambient exposure, particularly to air and moisture, which triggers the formation of toxic gases such as H$_2$S and H$_2$Se.[18] The surface of these materials degrades upon exposure,
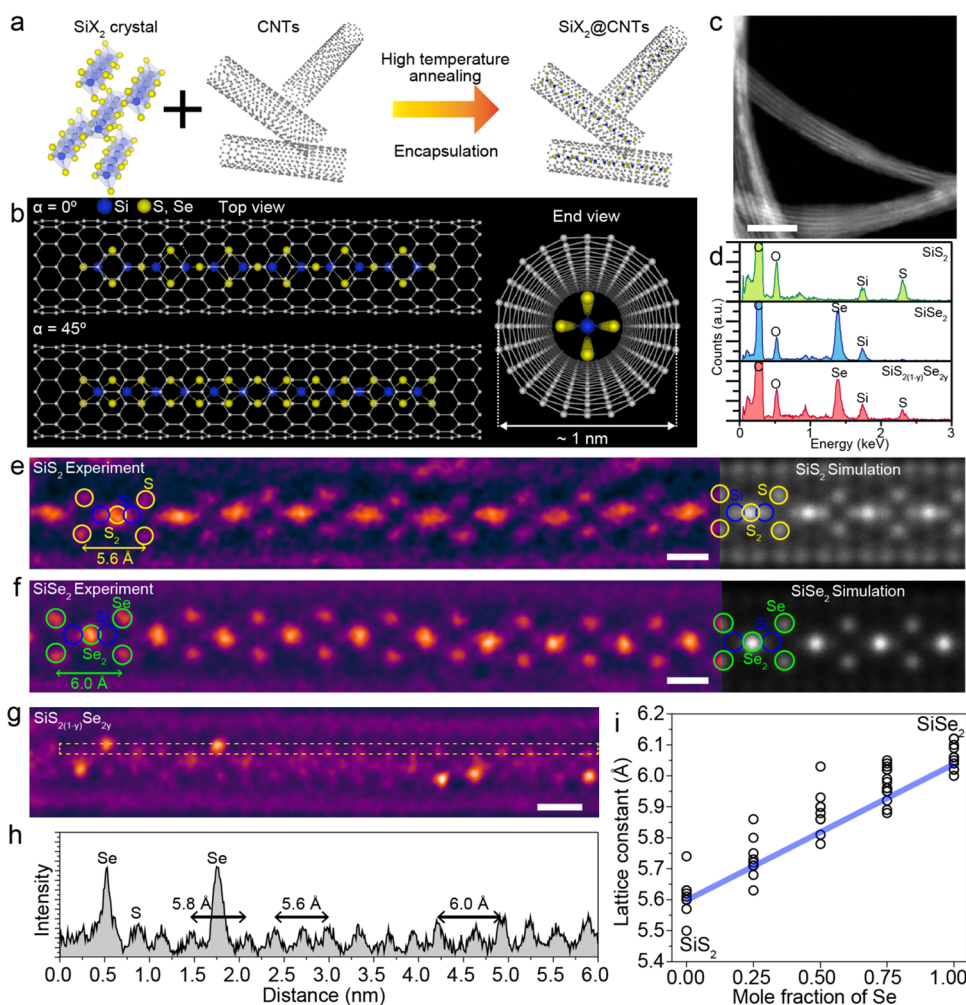
Figure 2. Isolation type-1 1D SiX_2 single chain inside nanotube. (a) Schematic of isolation of the 1D SiX_2 vdW chains via nanotube encapsulation. (b) Atomic model of type-1 SiX_2 single chain inside nanotube. (c) Low-magnification image of $SiSe_2$ encapsulated nanotube. Scale bar: 20 nm. (d) EDS spectra of SiS_2, $SiSe_2$, and $SiS_{2(1-y)}Se_{2y}$ alloy chains inside nanotubes. (e−g) Atomic-resolution STEM images of type-1 (e) SiS_2, (f) $SiSe_2$, and (g) $SiS_{2(1-y)}Se_{2y}$ alloy chain. Simulated STEM images of SiS_2 and $SiSe_2$ are shown on the right. Scale bar: 0.5 nm. (h) ADF intensity line profile of $SiS_{2(1-y)}Se_{2y}$ alloy chain inside the yellow square in panel (f). (i) Experimentally measured lattice constant versus Se fraction in the $SiS_{2(1-y)}Se_{2y}$ alloy sample.

resulting in the formation of bubbles, as shown in Figure S1. Additionally, the Raman spectrum of bulk SiX_2 distinctly shows a decrease in intensity following exposure to air. This high reactivity poses significant challenges in extending the production of SiS_2 and $SiSe_2$ to the single-chain limit and in further characterization.

We utilized a nanotube reaction vessel to isolate SiX_2 single chains and protect them from degradation (Figure 2a). SiX_2 chains in nanotube samples are synthesized by directly sublimating the SiX_2 precursors with open-ended nanotubes in sealed ampules, as described in the Methods section. Encapsulating SiX_2 in the nanotubes enables isolation of the material at the single-chain level and provides a high degree of environmental stability, thereby facilitating detailed characterization. Figure 2b illustrates the overall structure of the 1D SiX_2 single chain within the nanotube. The synthesized SiX_2 encapsulated nanotubes exhibit high filling fractions (approximately 90%) with chain lengths extending to hundreds of nanometers, as shown in Figures 2c and S2. The atomic composition ratio of SiS_2 and $SiSe_2$ is confirmed by energy-dispersive spectroscopy (EDS), which reveals a 1:2 atomic percentage ratio of Si to S or Se (Figure 2d). We also

synthesize a $SiS_{2(1-y)}Se_{2y}$ alloy chain inside the nanotubes, and EDS characterization confirms the coexistence of the S and Se from the sample. The average composition ratio of the alloy sample is $SiS_{0.8}Se_{1.2}$, as determined by EDS quantification.

The detailed atomic structure of the synthesized SiX_2 encapsulated nanotube samples is investigated using annular dark-field (ADF) aberration-corrected STEM. Figure 2e,f shows the atomic-resolution ADF-STEM image of SiS_2 and $SiSe_2$ single chain encapsulated in a nanotube with an inner diameter of 1 nm. The image contrast of ADF-STEM strongly depends on the atomic number (Z); thus, S ($Z_s = 16$) and Se ($Z_{se} = 34$) exhibit a higher intensity than Si ($Z_{si} = 14$). The simulated STEM images (right side in Figure 2e,f) are generated using the identified atomic structure, which matches well with the experimentally observed result. The observed 1D single-chain structure of SiS_2 and $SiSe_2$ in the nanotubes exhibits 1D chain structures with edge-shared tetrahedrons, which are identical to the single chains present in the bulk material, which we refer to as type-1 structure.[40] The atomic-resolution images of the 45° rotated SiS_2 and $SiSe_2$ chain structures within nanotubes also well match with our expected structure (Figure S3). The measured lattice constants of SiX_2
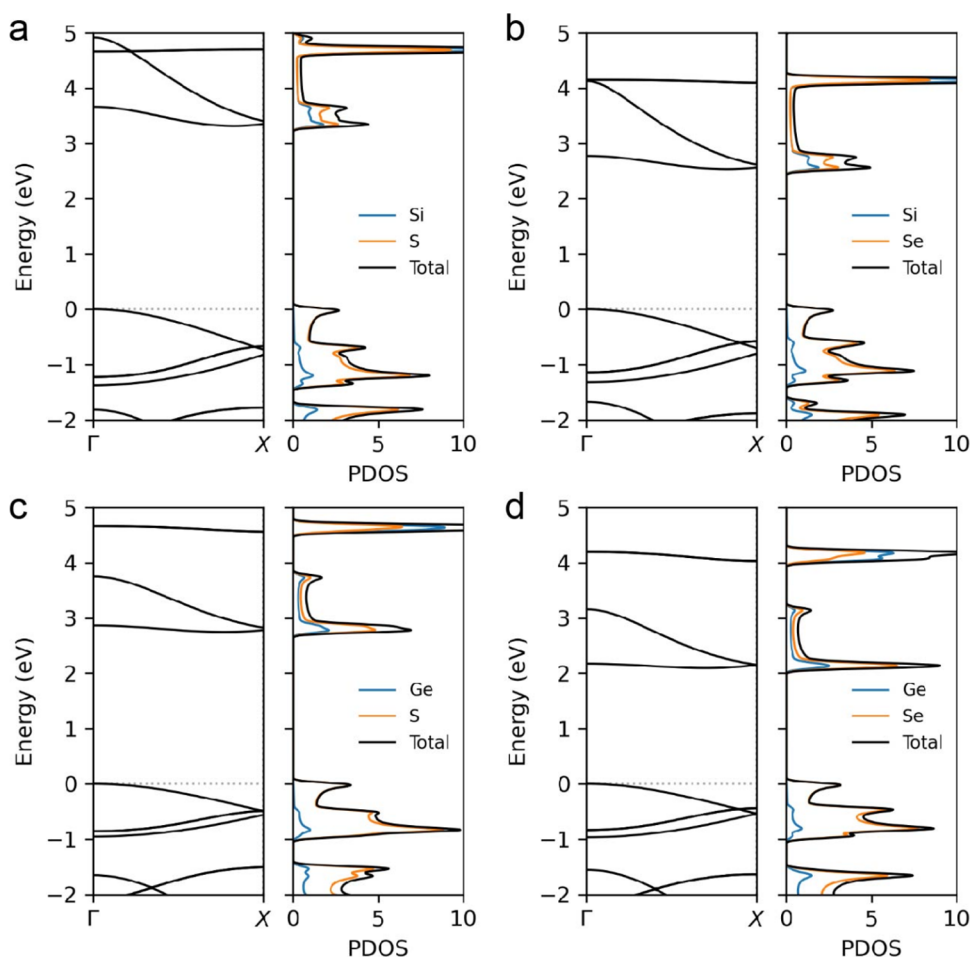
Figure 3. Calculated band structures and projected density of states (PDOS) of type-1 single chain. (a, b) SiX$_2$ (X = S and Se) and (c, d) GeX$_2$ for comparison. The valence bands mostly consist of chalcogen atomic orbitals, whereas the conduction bands states are distributed over all atoms.

chains along the chain directions are 5.6 Å for SiS$_2$ and 6.0 Å for SiSe$_2$, which are in good agreement with the previously reported chain distance from the bulk SiX$_2$ crystal structure.[15]

The SiS$_{2(1-y)}$Se$_{2y}$ ternary alloy sample maintains an identical chain structure within the nanotubes. Figure 2g shows an atomic-resolution ADF-STEM image of the type-1 SiS$_{2(1-y)}$Se$_{2y}$ alloy chain in a nanotube. Because of the higher atomic number of Se (Z_{se} = 34), the Se atomic positions are brighter than the S or Si atomic positions. Figure 2h shows the intensity line profile from the regions marked in Figure 2g, which clearly shows the intensity variation between Se and S. The larger atomic radius of Se compared to that of S leads to a modification in the lattice constant; for instance, the original lattice constant of SiS$_2$, 5.6 Å, increases to 5.8 Å with the substitution of one S atom for Se. As the mole fraction of Se increased, the lattice constant increased linearly and reached 6.0 Å, which is the lattice constant of SiSe$_2$. Figure 2i shows the experimentally measured lattice constant as a function of the Se fraction in SiSSe, showing linear behavior following Vegard's law. The substitution of S and Se in the SiSSe lattice may induce distortion and residual strain owing to the size mismatch between S and Se atoms. Despite the random distribution of chalcogenide atoms (S or Se) along the chains, they continue to preserve the edge-shared tetrahedral chain structure within the 1 nm diameter of the nanotubes. All of the

experimentally observed STEM images are in good agreement with the simulated STEM images, as shown in Figures S4−S6.

The internal diameter of the nanotube plays a crucial role in determining the confined structure. In a prior investigation, we discovered an alternative chain structure of GeX$_2$ in nanotubes with diameters ranging from 1.0 to 1.2 nm, called type-2.[40] This type-2 chain structure, featuring tetrahedral sharing edges and corners, deviates from the bulk GeX$_2$ structure. Similarly, we observed an identical type-2 SiX$_2$ chain structure in nanotubes with diameters ranging from 1.0 to 1.2 nm. Figure S7 shows the experimentally observed type-2 SiX$_2$ single chains inside the nanotubes, with atomic structures identical to those previously observed in the GeX$_2$ system.[40] Both the experimental and simulated STEM images of type-2 SiX$_2$ along various projection directions exhibit excellent agreement (Figures S8 and S9).

Other structures are also observed in the nanotubes with different diameters, as shown in Figure S10. Nanotubes with diameters less than 0.9 nm exhibit S or Se (even mixed case) single atomic-chain structures inside, whereas those with inner diameters larger than 1.2 nm result in the formation of multiple chains of SiX$_2$. These findings align with the previously studied diverse structures inside nanotubes of various diameters.[21,22,24,37,41−43] Our observations lead to the conclusion that the type-1 chain structure is stabilized in nanotubes with diameters ranging from 0.9 to 1.0 nm, whereas the type-2 chain
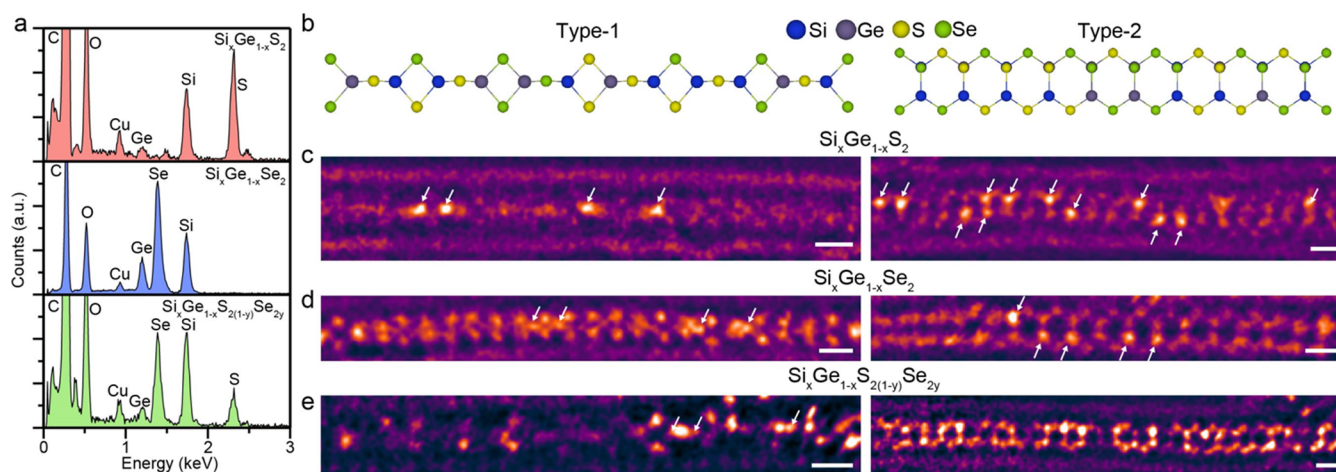
Figure 4. 1D $Si_xGe_{1-x}S_{2(1-y)}Se_{2y}$ alloy chain inside nanotube. (a) EDS spectra of $Si_xGe_{1-x}S_2$, $Si_xGe_{1-x}Se_2$, and $Si_xGe_{1-x}S_{2(1-y)}Se_{2y}$ alloy chains inside nanotubes. (b) Atomic model of (left) type-1 and (right) type-2 $Si_xGe_{1-x}S_{2(1-y)}Se_{2y}$ alloy chain structure. (c–e) Atomic-resolution STEM images of the (c) $Si_xGe_{1-x}S_2$, (d) $Si_xGe_{1-x}Se_2$, and (e) $Si_xGe_{1-x}S_{2(1-y)}Se_{2y}$ alloy single chain inside nanotube. Scale bar: 0.5 nm. White arrows indicate the atomic position of Ge.

structure is stabilized in nanotubes with diameters ranging from 1.0 to 1.2 nm (Figure S11).

We theoretically investigate the atomic structural and electronic properties of SiX_2 single chains using first-principles DFT calculations. The calculated lattice parameter along the axial direction is 5.68 and 6.00 Å for type-1 SiS_2 and $SiSe_2$, respectively, which are in good agreement with the experimental measurements. Figures 3 and S12 show the calculated electronic structures of SiX_2 chains as well as GeX_2 chains for comparison. All of the type-1 chains are indirect-gap semiconductors with the band gap of 3.31 and 2.53 eV for SiS_2 and $SiSe_2$, respectively. Conversely, the type-2 chains are identified as direct-gap semiconductors, with band gaps of 1.85 eV for SiS_2 and 1.22 eV for $SiSe_2$. In a single chain of SiX_2, the elimination of interactions between different chains leads to the absence of band dispersion in the plane perpendicular to the chains, resulting in a larger band gap than that of bulk SiX_2.[44] The valence bands predominantly consist of chalcogen atomic orbitals, while the conduction bands are spread across all atomic types. In our previous study, we found that CNT encapsulation did not markedly modify the atomic and electronic structures of GeX_2 chains, provided that there was no significant charge transfer between the GeX_2 chains and the CNTs.[40] Based on these observations, we assumed that the SiX_2 chains would exhibit similar behavior when encapsulated in CNTs. Therefore, all encapsulated chains, both SiX_2 and GeX_2, retain their semiconducting states.

Extending the aforementioned findings for SiX_2 and the previously studied GeX_2, we study the 1D $Si_xGe_{1-x}S_{2(1-y)}Se_{2y}$ quaternary single chains inside nanotubes with a different alloy composition, as shown in Figure 4. We synthesized various combinations of $Si_xGe_{1-x}S_{2(1-y)}Se_{2y}$ alloy chains inside nanotubes using mixed SiX_2 and GeX_2 precursors. The synthesized alloy samples are confirmed by EDS in STEM from a bundle of nanotubes. The EDS spectra exhibit well-defined peaks for each element (Si, Ge, S, and Se) in the $Si_xGe_{1-x}S_2$, $Si_xGe_{1-x}Se_2$, and $Si_xGe_{1-x}S_{2(1-y)}Se_{2y}$ alloy samples (Figure 4a). From the EDS quantitative analysis, the exemplary synthesized alloy samples are confirmed to be $Si_{0.7}Ge_{0.3}S_2$, $Si_{0.8}Ge_{0.2}Se_2$, and $Si_{0.9}Ge_{0.1}S_{0.4}Se_{1.6}$. Additionally, electron energy loss spectroscopy (EELS) is utilized to reveal the presence of Si, S, and Se

in the $Si_xGe_{1-x}S_{2(1-y)}Se_{2y}$ alloy within a single isolated nanotube (Figure S13). The Ge core-loss peak was not detected in the isolated nanotube sample because of the low Ge concentration in the quaternary alloy sample.

Given that both SiX_2 and GeX_2 form the same type of chain structure inside the nanotube, we expect the formation of type-1 (left side) and type-2 (right side) $Si_xGe_{1-x}S_{2(1-y)}Se_{2y}$ alloy chains, as shown in Figure 4b. Via successful synthesis and atomic-resolution STEM imaging, we observe both type-1 and type-2 chain structures in the $Si_xGe_{1-x}S_2$, $Si_xGe_{1-x}Se_2$, and $Si_xGe_{1-x}S_{2(1-y)}Se_{2y}$ samples (Figure 4c–e). In the ADF-STEM imaging, the Ge atomic positions exhibit a brighter contrast compared to those of Si and S, enabling the clear identification of Ge atoms in the $Si_xGe_{1-x}S_2$ alloy sample. In $Si_xGe_{1-x}Se_2$ and $Si_xGe_{1-x}S_{2(1-y)}Se_{2y}$, Se appears to be the brightest element. Contrast variations may occur based on the rotation of the chain structure and overlapping elements. For example, in 30° rotated type-2 $Si_xGe_{1-x}S_{2(1-y)}Se_{2y}$ (Figure 4e), the brightest atomic position corresponds to Ge + Se, and the darkest atomic position corresponds to Si + S. The STEM image simulations of both type-1 and type-2 are in good agreement with the experimentally observed image contrast variations (Figures S14−S17). Our study successfully demonstrates the synthesis of quaternary alloy chains at the single-chain limit via nanotube encapsulation.

Finally, we discuss the composition-dependent electronic structures of quaternary alloy chains. Figure 5 shows the calculated band gaps of type-1 $Si_xGe_{1-x}S_{2(1-y)}Se_{2y}$ alloy chains with different compositions. For a given composition, the atomic structures are linearly interpolated from the pure compositions of the chains: GeS_2 at ($x = 0$, $y = 0$), $GeSe_2$ at ($x = 0$, $y = 1$), SiS_2 at ($x = 1$, $y = 0$), and $SiSe_2$ at ($x = 1$, $y = 1$). We then calculate the electronic structure of the alloy chains using the virtual crystal approximation (VCA). The lower band gap regions, which are the blue regions in the figure, correspond to Ge-rich and Se-rich alloys, whereas the higher band gap regions in red correspond to Si-rich and S-rich alloys. This suggests that widely tunable band gaps, which are critical for atomic-scale optoelectronic applications, can be achieved by altering the ratios of Si, Ge, S, and Se in the single-chain limit.
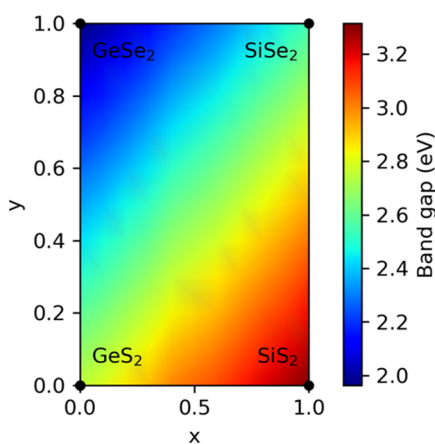
Figure 5. Band gap variation of the type-1 $Si_xGe_{1-x}S_{2(1-y)}Se_{2y}$ alloy chain as a function of composition. For a given composition, atomic structures and lattice parameters are linearly interpolated, and electronic structures are calculated by using the virtual crystal approximation.

CONCLUSIONS

In conclusion, we report the stabilization of 1D SiX_2 single chains via nanotube encapsulation. Our findings reveal that nanotube encapsulation stabilizes the materials and induces modifications in the chain structure of the confined material. Furthermore, we successfully demonstrate the synthesis and control of the composition of $Si_xGe_{1-x}S_{2(1-y)}Se_{2y}$ quaternary alloys at the single-chain level. Electronic structure calculations reveal that the band gap of these semiconducting alloy chains is highly adjustable and dependent on both the structural and the compositional ratio. These findings provide further groundwork for the study of low-dimensional and confinement-stabilized materials in nanotubes and offer opportunities for future research and applications in various fields.

METHODS

Materials. To synthesize SiS_2 and $SiSe_2$ precursors, we mixed silicon (99.999% Alfa Aesar) with sulfur (99.999% Alfa Aesar) or selenium (99.999% Alfa Aesar) in an atomic ratio of 1:2. The mixture (1g) was then sealed in a 10 mm diameter and 15 cm long ampule under high vacuum ($\sim 10^{-6}$ Torr) and placed in a horizontal one-zone furnace with the hot end at 850 °C for 5 days. After synthesis, the materials were extracted inside an Ar-filled glovebox to minimize oxidation. The GeS_2 and $GeSe_2$ powders were purchased from Ossila.

Growing SiX_2 and Alloy Chains @ Nanotube. CNTs were purchased from Sigma-Aldrich (single-walled: 704113) and Cheap Tubes (90% Single Walled-Double Walled (SW-DW) CNTs) and were annealed in air at 510 °C for 15 min to open the end caps. The open-ended CNTs (approximately 3 mg) were mixed with 20 mg of the precursor material and sealed in a 6 mm diameter and 15 cm long quartz ampule under a high vacuum ($\sim 10^{-6}$ Torr). The sealed ampule was then heated to 1000 °C in a single zone box furnace and kept there for 5 days before being cooled to room temperature for over 1 day. The synthesized materials (SiX_2@nanotube) were dispersed in isopropanol using a bath sonicator for 15 min and drop-cast onto lacey carbon Transmission Electron Microscopy (TEM) grids for STEM characterization. The alloy samples were also synthesized according to the procedure described above.

Optical Characterizations. Optical microscopy images were obtained using a Leica-DM750M inside an N_2-filled glovebox. Raman measurements were performed by using a Renishaw inVia confocal Raman microscope with a 514 nm laser under ambient conditions.

TEM/STEM Imaging and Simulations. TEM and STEM images were acquired using a double spherical (Cs) aberration-corrected JEOL ARM-200F operated at 80 kV. For atomic-resolution STEM imaging, a microscope was used with a 23 or 30 mrad convergence angle and collection semiangles ranging from 40−160 mrad.

Atomic-resolution STEM image simulations were performed by using MacTempas software based on multislice calculations. The simulation parameters were similar to the experimental parameters (e.g., a probe semiangle of 23 or 30 mrad, 0.05 Å/pixel sampling, and 20 frozen phonon calculations) for each simulation. Image analysis and processing were performed by using ImageJ software. Poisson noise was added to the simulated STEM images to match the experimental results.

EELS Characterizations. The STEM-EELS experiments were performed in a Nion HERMES microscope equipped with a C3/C5 corrector at an accelerating voltage of 60 kV. The beam convergence semiangle was 32 mrad, and the collection semiangle for EELS was 75 mrad, with the EELS aperture out.

Calculations. We performed first-principles DFT calculations as implemented in SIESTA.[45] We used the Perdew−Burke−Ernzerhof (PBE) functional,[46] norm-conserving pseudopotentials,[47] and a localized pseudoatomic orbital basis. van der Waals interactions were included within the Grimme-D2 scheme.[48] A real-space mesh cutoff of 500 Ry was used. We used a 25 Å thick cell along the transverse vacuum direction. The primitive Brillouin zone of the isolated chains was sampled by 12 k points. The atomic positions were optimized with a force threshold of 0.01 eV/Å. In the alloy calculations, we used the virtual crystal approximation by mixing the pseudopotentials of Si with Ge and S with Se, respectively.

ASSOCIATED CONTENT

Ⓢ Supporting Information

The Supporting Information is available free of charge at https://pubs.acs.org/doi/10.1021/acsnano.4c04184.

Optical images of the SiS_2 under ambient exposure; extra STEM characterizations of samples; including experimental atomic-resolution images and EELS characterizations; simulated STEM images; and DFT calculations for the electronic structure of type-2 SiX_2 and GeX_2 (PDF)

AUTHOR INFORMATION

Corresponding Authors

Yangjin Lee — *Department of Physics, University of California at Berkeley, Berkeley, California 94720, United States; Materials Sciences Division, Lawrence Berkeley National Laboratory, Berkeley, California 94720, United States; Department of Physics, Yonsei University, Seoul 03722, Korea; Center for Nanomedicine, Institute for Basic Science, Seoul 03722, Korea;* ⓘ orcid.org/0000-0001-7336-1198; Email: yangjinlee@yonsei.ac.kr

Kwanpyo Kim — *Department of Physics, Yonsei University, Seoul 03722, Korea; Center for Nanomedicine, Institute for Basic Science, Seoul 03722, Korea;* ⓘ orcid.org/0000-0001-8497-2330; Email: kpkim@yonsei.ac.kr

Alex Zettl — *Department of Physics, University of California at Berkeley, Berkeley, California 94720, United States; Materials Sciences Division, Lawrence Berkeley National Laboratory, Berkeley, California 94720, United States; Kavli Energy NanoSciences Institute at the University of California at Berkeley, Berkeley, California 94720, United States;* Email: azettl@berkeley.edu

Authors

Young Woo Choi — *Department of Physics, University of California at Berkeley, Berkeley, California 94720, United States; Materials Sciences Division, Lawrence Berkeley*

National Laboratory, Berkeley, California 94720, United States; ⓞ orcid.org/0000-0003-4725-1299

Linxuan Li − School of Physical Sciences and CAS Key Laboratory of Vacuum Physics, University of Chinese Academy of Sciences, Beijing 100049, People's Republic of China

Wu Zhou − School of Physical Sciences and CAS Key Laboratory of Vacuum Physics, University of Chinese Academy of Sciences, Beijing 100049, People's Republic of China

Marvin L. Cohen − Department of Physics, University of California at Berkeley, Berkeley, California 94720, United States; Materials Sciences Division, Lawrence Berkeley National Laboratory, Berkeley, California 94720, United States

Complete contact information is available at:
https://pubs.acs.org/10.1021/acsnano.4c04184

Author Contributions

Notes

ACKNOWLEDGMENTS

REFERENCES

(1) Geim, A. K. Graphene: Status and Prospects. Science 2009, 324, 1530−1534.

(2) Semonin, O. E.; Luther, J. M.; Beard, M. C. Quantum dots for next-generation photovoltaics. Mater. Today 2012, 15, 508−515.

(3) Kovalenko, M. V.; Manna, L.; Cabot, A.; Hens, Z.; Talapin, D. V.; Kagan, C. R.; Klimov, V. I.; Rogach, A. L.; Reiss, P.; Milliron, D. J.; Guyot-Sionnnest, P.; Konstantatos, G.; Parak, W. J.; Hyeon, T.; Korgel, B. A.; Murray, C. B.; Heiss, W. Prospects of Nanoscience with Nanocrystals. ACS Nano 2015, 9, 1012−1057.

(4) García de Arquer, F. P.; Talapin, D. V.; Klimov, V. I.; Arakawa, Y.; Bayer, M.; Sargent, E. H. Semiconductor quantum dots: Technological progress and future challenges. Science 2021, 373, eaaz8541.

(5) Gibertini, M.; Koperski, M.; Morpurgo, A. F.; Novoselov, K. S. Magnetic 2D materials and heterostructures. Nat. Nanotechnol. 2019, 14, 408−419.

(6) Kim, S. E.; Mujid, F.; Rai, A.; Eriksson, F.; Suh, J.; Poddar, P.; Ray, A.; Park, C.; Fransson, E.; Zhong, Y.; Muller, D. A.; Erhart, P.; Cahill, D. G.; Park, J. Extremely anisotropic van der Waals thermal conductors. Nature 2021, 597, 660−665.

(7) Jia, C.; Lin, Z.; Huang, Y.; Duan, X. Nanowire Electronics: From Nanoscale to Macroscale. Chem. Rev. 2019, 119, 9074−9135.

(8) Barrigón, E.; Heurlin, M.; Bi, Z.; Monemar, B.; Samuelson, L. Synthesis and Applications of III−V Nanowires. Chem. Rev. 2019, 119, 9170−9220.

(9) Quan, L. N.; Kang, J.; Ning, C.-Z.; Yang, P. Nanowires for Photonics. Chem. Rev. 2019, 119, 9153−9169.

(10) Zhu, Y.-H.; Yang, X.-Y.; Liu, T.; Zhang, X.-B. Flexible 1D Batteries: Recent Progress and Prospects. Adv. Mater. 2020, 32, 1901961.

(11) Wu, Y.; Zhao, X.; Shang, Y.; Chang, S.; Dai, L.; Cao, A. Application-Driven Carbon Nanotube Functional Materials. ACS Nano 2021, 15, 7946−7974.

(12) Balandin, A. A.; Kargar, F.; Salguero, T. T.; Lake, R. K. One-dimensional van der Waals quantum materials. Mater. Today 2022, 55, 74−91.

(13) Chen, M.; Li, L.; Xu, M.; Li, W.; Zheng, L.; Wang, X. Quasi-One-Dimensional van der Waals Transition Metal Trichalcogenides. Research 2023, 6, 0066.

(14) Zhu, Y.; Antoniuk, E. R.; Wright, D.; Kargar, F.; Sesing, N.; Sendek, A. D.; Salguero, T. T.; Bartels, L.; Balandin, A. A.; Reed, E. J.; da Jornada, F. H. Machine-Learning-Driven Expansion of the 1D van der Waals Materials Space. J. Phys. Chem. C 2023, 127, 21675−21683.

(15) Peters, J.; Krebs, B. Silicon disulphide and silicon diselenide: a reinvestigation. Acta Crystallogr., Sect. B: Struct. Crystallogr. Cryst. Chem. 1982, 38, 1270−1272.

(16) Tenhover, M.; Hazle, M. A.; Grasselli, R. K. Atomic Structure of SiS_2 and $SiSe_2$ Glasses. Phys. Rev. Lett. 1983, 51, 404−406.

(17) Griffiths, J. E.; Malyj, M.; Espinosa, G. P.; Remeika, J. P. Crystalline $SiSe_2$ and Si_xSe_{1-x} glasses: Syntheses, glass formation, structure, phase separation, and Raman spectra. Phys. Rev. B 1984, 30, 6978−6990.

(18) Chen, C.; Zhang, X.; Krishna, L.; Kendrick, C.; Shang, S.-L.; Toberer, E.; Liu, Z.-K.; Tamboli, A.; Redwing, J. M. Synthesis, characterization and chemical stability of silicon dichalcogenides, $Si(Se_xS_{1-x})_2$. J. Cryst. Growth 2016, 452, 151−157.

(19) Smith, B. W.; Monthioux, M.; Luzzi, D. E. Encapsulated C_{60} in carbon nanotubes. Nature 1998, 396, 323−324.

(20) Mickelson, W.; Aloni, S.; Han, W.-Q.; Cumings, J.; Zettl, A. Packing C_{60} in Boron Nitride Nanotubes. Science 2003, 300, 467−469.

(21) Sloan, J.; Kirkland, A. I.; Hutchison, J. L.; Green, M. L. H. Integral atomic layer architectures of 1D crystals inserted into single walled carbon nanotubes. Chem. Commun. 2002, 1319−1332.

(22) Senga, R.; Komsa, H.-P.; Liu, Z.; Hirose-Takai, K.; Krasheninnikov, A. V.; Suenaga, K. Atomic structure and dynamic behaviour of truly one-dimensional ionic chains inside carbon nanotubes. Nat. Mater. 2014, 13, 1050−1054.

(23) Pham, T.; Oh, S.; Stetz, P.; Onishi, S.; Kisielowski, C.; Cohen, M. L.; Zettl, A. Torsional instability in the single-chain limit of a transition metal trichalcogenide. Science 2018, 361, 263−266.

(24) Zhang, J.; Fu, C.; Song, S.; Du, H.; Zhao, D.; Huang, H.; Zhang, L.; Guan, J.; Zhang, Y.; Zhao, X.; Ma, C.; Jia, C.-L.; Tománek, D. Changing the Phosphorus Allotrope from a Square Columnar Structure to a Planar Zigzag Nanoribbon by Increasing the Diameter of Carbon Nanotube Nanoreactors. *Nano Lett.* **2020**, *20*, 1280−1285.

(25) Hart, M.; Chen, J.; Michaelides, A.; Sella, A.; Shaffer, M. S.; Salzmann, C. G. One-Dimensional Arsenic Allotropes: Polymerization of Yellow Arsenic Inside Single-Wall Carbon Nanotubes. *Angew. Chem.* **2018**, *130*, 11823−11827.

(26) Qin, J.-K.; Liao, P.-Y.; Si, M.; Gao, S.; Qiu, G.; Jian, J.; Wang, Q.; Zhang, S.-Q.; Huang, S.; Charnas, A.; Wang, Y.; Kim, M. J.; Wu, W.; Xu, X.; Wang, H.-Y.; Yang, L.; Khin Yap, Y.; Ye, P. D. Raman response and transport properties of tellurium atomic chains encapsulated in nanotubes. *Nat. Electron.* **2020**, *3*, 141−147.

(27) Gao, M.; Park, Y.; Jin, J.; Chen, P.-C.; Devyldere, H.; Yang, Y.; Song, C.; Lin, Z.; Zhao, Q.; Siron, M.; Scott, M. C.; Limmer, D. T.; Yang, P. Direct Observation of Transient Structural Dynamics of Atomically Thin Halide Perovskite Nanowires. *J. Am. Chem. Soc.* **2023**, *145*, 4800−4807.

(28) Kashtiban, R. J.; Patrick, C. E.; Ramasse, Q.; Walton, R. I.; Sloan, J. Picoperovskites: The Smallest Conceivable Isolated Halide Perovskite Structures Formed within Carbon Nanotubes. *Adv. Mater.* **2023**, *35*, 2208575.

(29) Kashtiban, R. J.; Burdanova, M. G.; Vasylenko, A.; Wynn, J.; Medeiros, P. V. C.; Ramasse, Q.; Morris, A. J.; Quigley, D.; Lloyd-Hughes, J.; Sloan, J. Linear and Helical Cesium Iodide Atomic Chains in Ultranarrow Single-Walled Carbon Nanotubes: Impact on Optical Properties. *ACS Nano* **2021**, *15*, 13389−13398.

(30) Lee, Y.; Choi, Y. W.; Lee, K.; Song, C.; Ercius, P.; Cohen, M. L.; Kim, K.; Zettl, A. One-Dimensional Magnetic MX_3 Single-Chains (M = Cr, V and X = Cl, Br, I). *Adv. Mater.* **2023**, *35* (49), 2307942.

(31) Teng, Y.; Zhang, Y.; Xie, X.; Yao, J.; Zhang, Z.; Geng, L.; Zhao, P.; Yang, C.; Gong, W.; Wang, X.; Hu, Z.; Kang, L.; Fang, X.; Li, Q. Interfacial Electron Transfer in PbI2@Single-Walled Carbon Nanotube van der Waals Heterostructures for High-Stability Self-Powered Photodetectors. *J. Am. Chem. Soc.* **2024**, *146*, 6231−6239.

(32) Wang, K.; Xia, G.-J.; Liu, T.; Yun, Y.; Wang, W.; Cao, K.; Yao, F.; Zhao, X.; Yu, B.; Wang, Y.-G.; Jin, C.; He, J.; Li, Y.; Yang, F. Anisotropic Growth of One-Dimensional Carbides in Single-Walled Carbon Nanotubes with Strong Interaction for Catalysis. *J. Am. Chem. Soc.* **2023**, *145*, 12760−12770.

(33) Nagata, M.; Shukla, S.; Nakanishi, Y.; Liu, Z.; Lin, Y.-C.; Shiga, T.; Nakamura, Y.; Koyama, T.; Kishida, H.; Inoue, T.; Kanda, N.; Ohno, S.; Sakagawa, Y.; Suenaga, K.; Shinohara, H. Isolation of Single-Wired Transition-Metal Monochalcogenides by Carbon Nanotubes. *Nano Lett.* **2019**, *19*, 4845−4851.

(34) Stonemeyer, S.; Dogan, M.; Cain, J. D.; Azizi, A.; Popple, D. C.; Culp, A.; Song, C.; Ercius, P.; Cohen, M. L.; Zettl, A. Targeting One-and Two-Dimensional Ta−Te Structures via Nanotube Encapsulation. *Nano Lett.* **2022**, *22*, 2285−2292.

(35) Cain, J. D.; Oh, S.; Azizi, A.; Stonemeyer, S.; Dogan, M.; Thiel, M.; Ercius, P.; Cohen, M. L.; Zettl, A. Ultranarrow TaS_2 Nanoribbons. *Nano Lett.* **2021**, *21*, 3211−3217.

(36) Meyer, S.; Pham, T.; Oh, S.; Ercius, P.; Kisielowski, C.; Cohen, M. L.; Zettl, A. Metal-insulator transition in quasi-one-dimensional $HfTe_3$ in the few-chain limit. *Phys. Rev. B* **2019**, *100*, 041403.

(37) Slade, C. A.; Sanchez, A. M.; Sloan, J. Unprecedented New Crystalline Forms of SnSe in Narrow to Medium Diameter Carbon Nanotubes. *Nano Lett.* **2019**, *19*, 2979−2984.

(38) Pham, T.; Oh, S.; Stonemeyer, S.; Shevitski, B.; Cain, J. D.; Song, C.; Ercius, P.; Cohen, M. L.; Zettl, A. Emergence of Topologically Nontrivial Spin-Polarized States in a Segmented Linear Chain. *Phys. Rev. Lett.* **2020**, *124*, 206403.

(39) Stonemeyer, S.; Cain, J. D.; Oh, S.; Azizi, A.; Elasha, M.; Thiel, M.; Song, C.; Ercius, P.; Cohen, M. L.; Zettl, A. Stabilization of $NbTe_3$, VTe_3, and $TiTe_3$ via Nanotube Encapsulation. *J. Am. Chem. Soc.* **2021**, *143*, 4563−4568.

(40) Lee, Y.; Choi, Y. W.; Lee, K.; Song, C.; Ercius, P.; Cohen, M. L.; Kim, K.; Zettl, A. Tuning the Sharing Modes and Composition in a Tetrahedral GeX_2 (X = S, Se) System via One-Dimensional Confinement. *ACS Nano* **2023**, *17*, 8734−8742.

(41) Eliseev, A. A.; Falaleev, N. S.; Verbitskiy, N. I.; Volykhov, A. A.; Yashina, L. V.; Kumskov, A. S.; Zhigalina, V. G.; Vasiliev, A. L.; Lukashin, A. V.; Sloan, J.; Kiselev, N. A. Size-Dependent Structure Relations between Nanotubes and Encapsulated Nanocrystals. *Nano Lett.* **2017**, *17*, 805−810.

(42) Fujimori, T.; Morelos-Gómez, A.; Zhu, Z.; Muramatsu, H.; Futamura, R.; Urita, K.; Terrones, M.; Hayashi, T.; Endo, M.; Hong, S. Y.; Choi, Y. C.; Tománek, D.; Kaneko, K. Conducting linear chains of sulphur inside carbon nanotubes. *Nat. Commun.* **2013**, *4*, 2162.

(43) Fujimori, T.; dos Santos, R. B.; Hayashi, T.; Endo, M.; Kaneko, K.; Tománek, D. Formation and Properties of Selenium Double-Helices inside Double-Wall Carbon Nanotubes: Experiment and Theory. *ACS Nano* **2013**, *7*, 5607−5613.

(44) Cui, J.; Yang, W.; Cheng, Y.; Dong, H.; Liu, H.; Zuo, X.; Wang, W.-H.; Lu, F. Electronic states, mechanical properties and doping effects of one-dimensional atomic wires of SiX_2 (X = S, Se). *Appl. Surf. Sci.* **2021**, *559*, 149894.

(45) Soler, J. M.; Artacho, E.; Gale, J. D.; García, A.; Junquera, J.; Ordejón, P.; Sánchez-Portal, D. The SIESTA method for ab initio order- N materials simulation. *J. Phys.: Condens. Matter* **2002**, *14*, 2745−2779.

(46) Perdew, J. P.; Burke, K.; Ernzerhof, M. Generalized Gradient Approximation Made Simple. *Phys. Rev. Lett.* **1996**, *77*, 3865−3868.

(47) Oroya, J.; M, A.; Callejo, M.; Garcia-Mota, M.; Marchesin, F. *Pseudopotential and Numerical Atomic Orbitals Basis Dataset*, www.simuneatomistics.com. (accessed January 14, 2022).

(48) Grimme, S. Semiempirical GGA-type density functional constructed with a long-range dispersion correction. *J. Comput. Chem.* **2006**, *27*, 1787−1799.